

## Cosmic Ray Spectrum Steepening in Supernova Remnants - I. Loss-Free Self-Similar Solution

M.A. MALKOV<sup>1</sup> AND F.A. AHARONIAN<sup>2,3</sup>

<sup>1</sup>*Department of Physics and CASS, University of California San Diego*

<sup>2</sup>*Dublin Institute for Advanced Studies, 31 Fitzwilliam Place, Dublin 2, Ireland*

<sup>3</sup>*Max-Planck-Institut für Kernphysik, P.O. Box 103980, D 69029 Heidelberg, Germany*

### Abstract

The direct measurements of cosmic rays (CRs), after correction for the propagation effects in the interstellar medium, indicate that their source spectra are likely to be significantly steeper than the canonical  $E^{-2}$  spectrum predicted by the standard Diffusive Shock Acceleration (DSA) mechanism. The DSA has long been held responsible for the production of galactic CRs in supernova remnant (SNR) shocks. The  $\gamma$ -ray "probes" of the acceleration spectra of CRs on-the-spot, inside of the SNRs, lead to the same conclusion. We show that the steep acceleration spectrum can be attributed to the *combination* of (i) spherical expansion, (ii) tilting of the magnetic field along the shock surface and (iii) shock deceleration. Because of (i) and (ii), the DSA is efficient only on two "polar caps" of a spherical shock where the local magnetic field is within  $\simeq 45^\circ$  to its normal. The shock-produced spectrum observed edge-on steepens with the particle energy because the number of freshly accelerated particles with lower energies continually adds up to a growing acceleration region. We demonstrate the steepening effect by obtaining an exact self-similar solution for the particle acceleration at expanding shock surface with an arbitrary energy dependence of particle diffusivity  $\kappa$ . We show that its increase toward higher energy steepens the spectrum, which deeply contrasts with the standard DSA spectrum where  $\kappa$  cancels out.

### 1. INTRODUCTION

It is believed that the relativistic particles, electrons, protons and nuclei, measured locally in the Solar System, represent, at least up to  $E \sim 10^{15}$  eV, the so-called Galactic component of CRs. The flux of these particles is determined by the overall rate of injection of CRs into the interstellar medium (ISM) and by their confinement time in the Galactic Disk,  $\tau$ . Because of the energy-dependent propagation, the energy spectrum of CRs in the Galactic Disk is modified and significantly deviates from the average source (acceleration) spectrum. The latter is recovered from the energy distribution of primary cosmic rays  $dN/dE \propto E^{-2.75-2.85}$ , and the energy dependence of the confinement  $\tau(E) \propto E^{-\delta}$ , with  $\delta \sim 0.3-0.5$  as it follows from the independently reported CR secondary-to-primary ratio. The resulting mismatch between the source spectrum, ought to be in the range  $E^{-2.25} - E^{-2.55}$ , and the "nominal"  $E^{-2}$  type spectrum predicted by the standard Diffusive Shock Acceleration (DSA) theory, can no longer be attributed to the statistical or systematic errors in observations. Indeed, the latter now reliably produce CR spectral indices with up to three-digit precision in relevant energy ranges. Moreover, it is becoming increasingly evident that  $\gamma$ -ray observations, which provide a powerful tool for the *in situ* probes of energy distributions of CRs inside the accelerators, also point to a similar discrepancy. Despite the DSA predictions, most of SNRs, including very young objects like SN 1006, Tycho, and Cas A, show fairly steep spectra (Aharonian et al. 2018). Instead of a single  $E^{-2}$ -type spectrum stretching all the way to the maximum energy, which would serve as a signature of the DSA, we often see softer spectra showing a gradual steepening. This discrepancy is a growing concern in the CR community, reflected, e.g., in a recent review by Gabici et al. 2019<sup>1</sup>.

Logically, such disagreement may be attempted to settle by tweaking the DSA theory. However, the DSA is remarkably insensitive to factors other than the shock compression as long as no strong backreaction of accelerated particles on the shock itself is expected. To make matters worse, such backreaction generally leads to harder rather than softer spectra for energies exceeding several GeV. Indeed, an analytic solution incorporating the backreaction has a *concave* spectrum tending to  $E^{-3/2}$  at high energies, in the limit of strong shocks and maximum energy in the TeV range (Malkov & Drury 2001). This trend is clearly in conflict with the *convex* spectra inferred from the  $\gamma$ -emission in a

<sup>1</sup> Short after our manuscript was accepted for publication, a new paper addressing this same issue was posted, (Bell et al. 2019)

number of SNRs. We will return to the nonlinear shock modification and some other aspects of the DSA, which can potentially alter the  $E^{-2}$  spectrum, in the Discussion section.

It follows that the above constraints on the acceleration spectra may point to some DSA physics not included in standard treatments. In particular, we will demonstrate that the spectral index  $q$ , and the maximum (cutoff) momentum,  $p_{\max}$ , are not exhaustive parameters for the DSA theory, under acceleration conditions outlined below and explained further in the paper. Even if  $p_{\max}$  can be regarded as adjustable, given the limited acceleration time and shock size, the power-law index  $q$  is a robust DSA prescription:  $f_{CR} \propto p^{-q}$  (we will use  $p$  instead of  $E$ , so that  $p^{-q}$  corresponds to  $E^{2-q}$ ). The index  $q$  merely depends on the Mach number,  $M$ , but only weakly so if the shock is strong,  $q \approx 4/(1 - M^{-2})$ ; note that the bulk of the galactic CRs are thought to come namely from strong shocks. Most of the DSA treatments, however, apply to planar, slowly evolving (over the acceleration timescale) shocks. Although spherically expanding shocks have also been studied, they were approximated by isotropic, essentially 1D (radial) configurations, e.g., (Prishchep & Ptuskin 1981; Berezhko et al. 1994; Drury 2011) (see, however, Völk et al. (2003); Pais et al. (2018)). The overall production spectrum in such shocks remains similar to the planar DSA predictions, with a possible exception of the work by Drury (2011) whose phenomenological “box” model has the potential for spectral steepening. However, the box model incurs the loss of information due to spatial integration, so the obtained particle spectrum contains undetermined parameters.

This paper is an attempt to remodel the DSA for capturing three-dimensional aspects of shock interaction with the ambient magnetic field. Assuming spherical shock geometry and a homogeneous ambient magnetic field, one may see that particle acceleration conditions change on any given field line crossing the shock surface. This is because the angle  $\vartheta_{nB}$  that the field line makes with the shock normal decreases with time. Particle injection (and to some extent their subsequent acceleration) becomes efficient when  $\vartheta_{nB}$  decreases below some critical value,  $\vartheta_{nB} \lesssim \vartheta_{cr} \approx \pi/4$ . Our objective is to understand the impact of this continuous transition on the integrated CR spectra and, by implication, on the instantaneous line-of-sight ones. Besides the  $\vartheta_{nB}$  variation, we also include the effects of shock expansion and deceleration. The time dependence of the DSA comes then in two flavors: the shock’s slow down and continuous addition of freshly accelerated (low-energy) particles to those field lines that just began to make its angle  $\vartheta_{nB} \lesssim \pi/4$ .

Effects of magnetic field inclination and time-dependence make the DSA spectrum *convex*, which we will demonstrate using a closed-form self-similar solution for an SNR expanding into a homogeneous magnetic field. Integrating the convection-diffusion equation across the field makes the problem effectively one-dimensional, but strongly time-dependent with the 3D effect of magnetic field inclination included. As *particle losses are neglected*, this solution produces a minimum steepening effect, caused exclusively by the *momentum dependence of particle diffusion*. By contrast, the loss-free DSA solution for a steadily propagating planar shock is fundamentally independent of the particle diffusion rate because it cancels out from the balance of spatial and momentum transport terms (see also Sec.6 below).

While not addressing the particle losses directly, this paper sets out a framework for studying an additional spectrum steepening caused by them. The losses may be incurred in the following ways:

- direct escape of particles from the acceleration zone along the field lines by reaching its boundary where both the turbulence and particle self-confinement are weak, (Malkov et al. 2013; Nava & Gabici 2013; D’Angelo et al. 2016)
- crossfield particle diffusion toward the edge of acceleration zone ( $\vartheta_{nB} \approx \vartheta_{cr}$ ) with a subsequent rapid escape along the field lines due to insufficient particle self-confinement in the region  $\vartheta \gtrsim \vartheta_{cr}$  (this scenario is briefly considered in the paper and studied in detail by Hanusch et al., prepared for submission to ApJ)
- crossfield expansion of the acceleration zone driven by the pressure of accelerated particles and possibly amplified magnetic field

The focus of this paper is on a probably not very large subset of SNRs with a bilateral morphology, best exemplified by the SNR 1006. At the same time, this type of SNRs, and especially the 1006, is an excellent laboratory to study the DSA, as it links the magnetic field direction with the acceleration efficiency all around the SNR shell. Particle acceleration in more complex SNRs with a less regular ambient field can hardly be understood without a grasp of the DSA operation in simple bilateral remnants. Indeed, turbulent ISM field with sufficiently large correlation length being intersected by a shock front (even if it is planar) will exhibit local alternation between injection and non-injection shock areas, similar to that observed in SNR 1006 at the scale of the entire remnant. We will also return to such possibility in the Discussion section. The paper is structured as follows: Sec.2 discusses modifications to the DSA

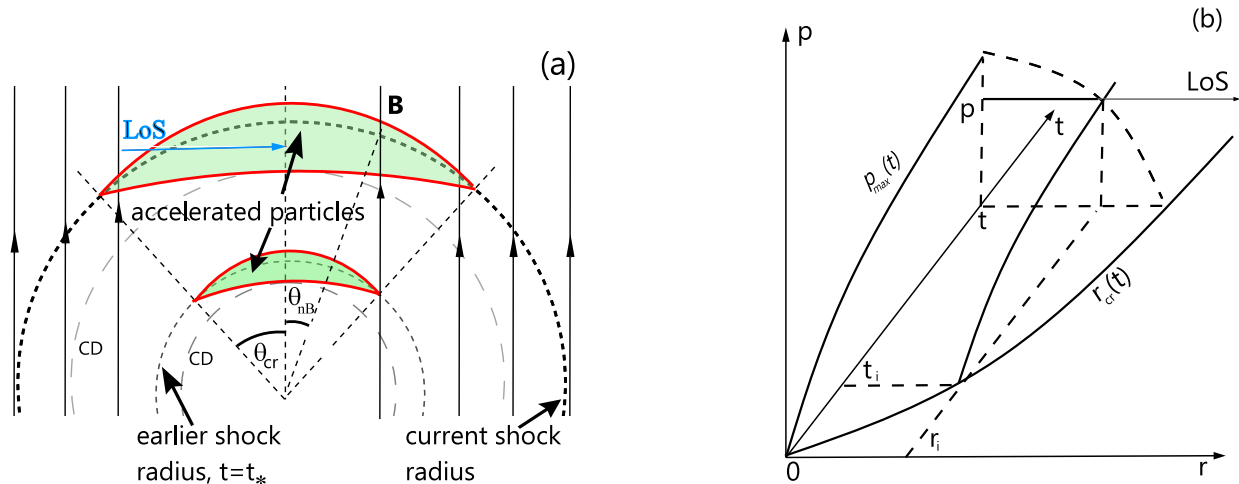


**Figure 1.** (a) A half of the spherical shock surface expanding into an ISM plasma with a constant magnetic field. The shock surface is shown at two different times. The long-dashed line circles indicate the respective positions of the contact discontinuity, CD. An opposite side of the remnant with a symmetric shock-field alignment is not shown. (b) CR production in expanding active acceleration zone  $r \leq r_{\text{cr}}(t)$ , where  $r$  is counted from the magnetic axis  $\vartheta = 0$  along the shock front. Particles started their acceleration at  $t = t_i$ ,  $r = r_i$  do not contribute to the spectrum between  $p$  and  $p_{\text{max}}(t)$  by the time  $t$ . This makes the spectrum integrated along the LoS softer than the local spectrum at any fixed  $r < r_{\text{cr}}(t) \equiv R_s(t) \sin \vartheta_{\text{cr}}$ , since the length of the LoS (heavy-line portion of it) is becoming progressively shorter with growing particle momentum.

theory for a spherical shock propagation in a constant magnetic field. In Sec.3 a convection-diffusion equation for particle acceleration is introduced, along with some simplifications of the shock geometry, whereas its solution is obtained in Sec.4. After reviewing its limiting cases in Sec.5 and comparing the results with those of the standard DSA in Sec.6, including particle escape, the paper concludes with a brief summary and discussion in Secs.7 and 8.

## 2. DSA MECHANISM WITH EVOLVING SHOCK OBLIQUITY

### 2.1. Particle Acceleration Domain on the Shock Surface

The spectral softening mechanism considered in this paper is illustrated in Fig.1. The two crescent regions in Fig.1a show that part of a spherical shock where the DSA works efficiently. This active acceleration zone is presented at two separate times to show in Sec.2.2 below how the spectrum sampled along the line of sight may appear steeper than the one at any given field line. Shock-accelerated particles are concentrated at this expanding region because the proton injection is efficient only where the shock normal makes a reasonably sharp angle,  $\vartheta_{nB}$ , with the local magnetic field direction (quasi-parallel shock geometry), assumed vertical in the figure. The critical angle  $\vartheta_{nB} = \vartheta_{\text{cr}}$ , beyond which the proton injection rate into the DSA drops sharply, is close to  $\vartheta_{\text{cr}} \simeq \pi/4$ . This choice of the source for particle injection is supported by simple theoretical considerations (Malkov & Völk 1995; Völk et al. 2003), as well as Monte-Carlo (Ellison et al. 1995) and hybrid simulations, e.g., (Thomas & Winske 1990; Caprioli & Spitkovsky 2014). A simple explanation is that for larger  $\vartheta_{nB}$  the recession of the field line - shock intersection point is too fast for the downstream particles to return upstream and continue acceleration. Most importantly, this pattern of particle acceleration is supported by observations (Long et al. 2003).

While the shock radius increases, the accelerated particles fill up an expanding disc-like layer near the shock surface intersecting a cone with a constant opening angle  $\approx \vartheta_{\text{cr}}$ . This layer consists of two parts separated by the shock surface: the shock precursor, of the size  $\kappa(p_{\text{max}})/U_{\text{sh}}$ , and the post-shock region occupied by the accelerated particles convected downstream. (Here  $\kappa$  is the particle diffusivity and  $U_{\text{sh}}$  is the shock speed.) The thicknesses of these layers also grow in time; the precursor grows due to an increase in the maximum momentum,  $p_{\text{max}}(t)$ , under a balance of particle diffusion away from the shock while the shock is catching them up. It also grows because of a decreasing shock speed. In the case of Bohm regime, the particle diffusion coefficient scales linearly with  $p \gg mc$ , as  $\kappa \simeq \kappa_B \equiv cr_g/3$ , where  $r_g$  is the particle gyro-radius and  $c$  is the speed of light. The thickness of the downstream particle layer is also determined by diffusion and convection. However, by contrast with the upstream layer they act in the same direction:

the convective growth of the layer,  $L_{conv} \sim U_{sh}(t - t_i)/\sigma$ , is extended by a trailing sub-layer across which the density of accelerated particles drops to its background (e.g., zero) level. The particle transport across this sub-layer (along the field) is self-regulated by Alfvén waves excited by particles escaping downstream from the shocked plasma. The time  $t_i = t_i(\vartheta, R)$  signifies the beginning of acceleration on a given field line crossed by the shock at the critical angle  $\vartheta_{cr}$ . The shock compression  $\sigma$  in the above expression for  $L_{conv}$  accounts for the slow down of the upstream flow upon the shock crossing. Time-asymptotically, when the far downstream side of this particle sub-layer is disconnected from the shock, a self-similar solution obtained by (Malkov et al. 2013) applies. In this paper, however, we do not take into account this latter aspect of particle transport and focus on the anisotropic magnetic environment, essential for the CR production spectrum but disregarded in previous studies. The above brief description of particle transport upstream and downstream of the shock will be useful in constructing time-dependent self-similar solution.

## 2.2. Spectrum Steepening Mechanism

When the particle acceleration zone near a shock is seen edge-on, which is typical because of a greatly enhanced emissivity, the line-of-sight (LoS) integrated emission is sampled from particles with different acceleration history, depending on their distance from the magnetic axis ( $\vartheta = 0$ ); it is the longest at  $\vartheta = 0$ . Farther away from the magnetic axis of the remnant, where  $\vartheta$  approaches  $\vartheta_{nB} \simeq \vartheta_{cr}$ , the freshly accelerated particles contribute to lower momenta of the observed spectrum, Fig.1b, because of the shorter duration of acceleration on the field lines near  $\vartheta_{cr}$ . They make thus the LoS-integrated spectrum steeper by enriching its low-energy part.

To demonstrate the spectrum steepening caused by the shock geometry, consider an idealized case when the freshly injected particles undergo shock acceleration but remain on the same field line (do not diffuse along the shock front). This assumption is justified (at least for  $t \lesssim \tau_a \sim \kappa_{\parallel}/U_{sh}^2$ ) because the diffusion length along the field line (shock precursor scale)  $L_p \sim \kappa_{\parallel}/U_{sh} \ll r_{cr} \sim R_s$ , so that the lateral displacement during the acceleration time  $\tau_a \sim \kappa_{\parallel}/U_{sh}^2$  is  $L_{\perp} \sim \sqrt{\kappa_{\perp}\tau_a} = \sqrt{\kappa_{\perp}\kappa_{\parallel}}/U_{sh} \sim \kappa_B/U_{sh} \sim L_p \ll r_{cr}$ . Apart from the normalization, unimportant here, the spectrum with an abrupt cutoff at  $p_{max}$  at any given field line at a distance  $r$  from the axis is

$$f(p, r) = p^{-q} H(p_{max}(r) - p)$$

where  $H$  is the Heaviside unit function, and  $p_{max}$  is the maximum momentum at the distance from magnetic axis,  $r \approx R_s \sin \vartheta_{nB}$ , Fig.1. Assuming Bohm diffusion and a ballistic shock expansion, which implies  $p_{max}(r = 0, t) \propto r_{cr}(t) \propto t$ , we can write  $p_{max}(r) = p_{max}(0, t)(1 - r/r_{cr})$ . We can then define the following spatially averaged spectrum

$$F_l(p) = \frac{1}{r_{cr}^{l+1}} \int_0^{r_{cr}} r^l f(p, r) dr$$

where  $l = \{0, 1\}$  for a LoS-averaged ( $l = 0$ ) spectrum or shock-area integrated one ( $l = 1$ ). Note that the latter case is more closely related to the cumulative CR production and will be considered in detail in the next section. It is also clear that the effect of spectral steepening caused by addition of freshly injected particles at  $r \approx r_{cr}$  is stronger in this case. Substituting the above expressions for  $f$  and  $p_{max}$ , and assuming that (locally) the DSA produces the spectrum  $\propto p^{-q}$ , with  $q = 3\sigma/(\sigma - 1)$ , where  $\sigma$  is the shock compression ratio, we find

$$F_l(p) = \frac{p^{-q}}{l+1} \left(1 - \frac{p}{p_{max}(0)}\right)^{l+1}$$

For  $p \ll p_{max}(0)$ , the latter result can be written as

$$F_l(p) \approx \frac{1}{l+1} p^{-q} \exp\left[-(l+1) \frac{p}{p_{max}(0)}\right]$$

The last expression shows that the standard DSA spectrum  $p^{-q}$  steepens with momentum and can even mimic an incipient exponential cut-off if observed at moderately high momenta. In the next section we take a more systematic approach to this effect by including also the particle cross-field diffusion and time dependent shock evolution.

## 3. EQUATION FOR PARTICLE ACCELERATION

Since the direction of magnetic field relative to the shock normal is key for particle injection, it is convenient to use a cylindrical coordinate system,  $(r_{\perp}, z)$ , with  $\mathbf{B} \parallel \hat{\mathbf{z}}$ , where  $\hat{\mathbf{z}}$  is the unit vector along the  $z$ -axis passing through the

center of the remnant. The overall shock morphology in such remnants as SNR 1006 and Tycho is spherical, but at least the 1006 appearance is distinctively different in the areas of quasi-parallel and quasi-perpendicular shock geometry ( $\vartheta_{nB} \ll 1$  and  $\pi/2 - \vartheta_{nB} \ll 1$ , respectively). In the NE and SW regions of the 1006, large portions of the shock surface are flattened, if not slightly concave or at least corrugated, as we can guess from our vista point, (Long et al. 2003; Bamba et al. 2005; Cassam-Chenaï et al. 2008). The overall shock morphology is therefore a barrel-shaped rather than spherical, with the equatorial part resembling a cylindrical surface rather than spherical shell. Since the active acceleration zones coincide with two *flattened* polar caps, we can ascribe two unique values to the respective shock coordinates,  $z = \pm z_s(t)$ , assumed independent of the radial coordinate,  $r_\perp$ . The radial extent of that portion of the shock surface where the particle acceleration is efficient is limited by the critical angle  $\vartheta_{nB} = \vartheta_{cr} \simeq \pi/4$ , which justifies the locally planar shock approximation. The convection-diffusion equation for particles undergoing acceleration in the layer near  $z = z_s(t)$  and  $r_\perp \leq r_{cr}(t) = R_s(t) \sin \vartheta_{cr}$  takes the following form

$$\frac{\partial f}{\partial t} + u \frac{\partial f}{\partial z} - \frac{\partial}{\partial z} \kappa_\parallel \frac{\partial f}{\partial z} - \frac{1}{r_\perp} \frac{\partial}{\partial r_\perp} r_\perp \kappa_\perp \frac{\partial f}{\partial r_\perp} - \frac{1}{3} \frac{\partial u}{\partial z} p \frac{\partial f}{\partial p} = Q(r_\perp, t) \delta(z) \delta(p - p_0) \quad (1)$$

Here we shifted the origin of  $z$ -coordinate to the shock position,  $z \rightarrow z_s(t) + z$ . The above equation is distinct from those typically used for particle acceleration in that it includes an additional cross-field transport with the particle diffusivity  $\kappa_\perp$ . This term is needed here because, by contrast to one-dimensional treatments with the constant injection rate along the shock surface, the injection intensity  $Q(r_\perp)$  vanishes at  $r_\perp \gtrsim r_{cr}(t)$ , while the injection area grows as the shock expands and  $r_{cr}$  increases. Already for this reason, the *acceleration process is fundamentally time-dependent*. The above equation is written in the shock frame. Although this frame is not inertial, since  $\dot{z}_s = u_{shock} \neq const$ , eq.(1) describes a mass-less CR-fluid diffusively coupled to the local flow, so it is valid for  $u = u(t)$ . Here  $p_0$  refers to the particle injection momentum.

#### 4. LOSS-FREE TIME-DEPENDENT SPECTRUM OF ACCELERATED PARTICLES

Now we focus on the solution of eq.(1) that determines both the emission spectrum of accelerated particles observed along the line of sight, as shown in Figs.1a,b, and a CR production spectrum integrated over the active life of an SNR shock in question. In this paper, we will address the latter task by calculating a radially integrated spectrum. It is a good proxy for the LoS-integrated spectrum, but they are not identical except when the local spectrum is radially independent. The radially integrated spectrum can be derived from eq.(1) directly.

##### 4.1. Radially integrated spectrum

As we pointed out in the preceding section, the particle density presumably vanishes at the critical radius,  $r_\perp = r_{cr}(t)$ . Therefore, we may extend the integration to infinity, thus introducing an integrated spectrum and the source of injected particles as

$$\bar{F}(z, p, t) = 2\pi \int_0^\infty r_\perp f(z, r_\perp, p, t) dr_\perp \quad \text{and} \quad S(t) = 2\pi \int_0^\infty r_\perp Q(r_\perp, t) dr_\perp, \quad (2)$$

With these definitions, from eq.(1) we obtain

$$\frac{\partial \bar{F}}{\partial t} + u \frac{\partial \bar{F}}{\partial z} - \frac{\partial}{\partial z} \kappa_\parallel \frac{\partial \bar{F}}{\partial z} = \frac{1}{3} \frac{\partial u}{\partial z} p \frac{\partial \bar{F}}{\partial p} + S(t) \delta(z) \delta(p - p_0). \quad (3)$$

It is implied here, that  $u$  and  $\kappa_\parallel$  do not depend on  $r_\perp$ . This assumption is acceptable for  $\kappa_\parallel$  only in the area of particle localization,  $r_\perp \leq r_{cr}$ . The parallel diffusion strongly increases outside of this area where the turbulence level is expected to be much lower. Conversely, the perpendicular transport strongly decreases beyond the point  $r_\perp = r_{cr}$ . The interface between different propagation regimes near  $r_\perp = r_{cr}$ , which in general is  $p$  and  $z$ -dependent, deserves a separate study. Here, we assume that the particle density drops beyond  $r_\perp = r_{cr}$  sharply, and accept the value  $\kappa_\parallel(r_\perp < r_{cr}) \approx const$  in eq.(3), but allow for an arbitrary momentum dependence,  $\kappa_\parallel(p)$ . We will also neglect its strong enhancement that potentially can result in fast particle losses along the field line in the area  $r_\perp \gtrsim r_{cr}$ . Based on this assumption, the radially integrated convection-diffusion equation, eq.(3) does not contain radial losses (see, however, Sec.6). Its solution will thus constitute the flattest possible, loss-free spectrum. Yet as we will see, the spectrum shows an evident rollover towards higher momenta due to the time-dependent acceleration effects discussed in Sec.2. The neglected losses would further steepen the spectrum, which we plan to address in a separate publication. Next, we discuss what stage of an SNR expansion is most relevant to our subject.

#### 4.2. Selection and Description of the SNR Expansion Stage

From the known stages of SNR dynamical evolution (Chevalier 1977; Bisnovatyi-Kogan & Silich 1995; McKee & Truelove 1995), the strongest impact on the CR production must have the ejecta-dominated (ED) and Sedov-Taylor (ST) stages. The shock radius grows linearly,  $R_s \propto t$ , during the ED stage, and slows down considerably during the ST stage,  $R_s \propto t^{2/5}$ . The transition between the two is smooth, nominally occurring at  $t \sim t_{ST}$ , which we will further denote by  $t_0$ , thus only loosely associating it with the commonly defined quantity,  $t_{ST} \approx 0.495 M_e^{5/6} / \rho_0^{1/3} \sqrt{E} \approx 209 (M_e/M_\odot)^{5/6} / n_0^{1/3} \sqrt{E_{51}}$ . Here  $M_e$  and  $M_\odot$  are the ejecta and solar masses, respectively,  $E$  is the ejecta energy (given in  $10^{51}$  erg units  $E_{51}$ ),  $n_0 = \rho_0 / 2.34 \times 10^{-24}$  g, with  $\rho_0$  being the ambient mass density. McKee & Truelove (1995) give a convenient analytic fit to the actual hydrodynamic solution of an SNR expansion problem well describing the first two stages of expansion:

$$R_s = R_{ST} \begin{cases} 1.37t (1 + 0.6t^{3/2})^{-2/3}, & t < 1 \\ (1.56t - 0.56)^{2/5}, & t > 1 \end{cases} \quad (4)$$

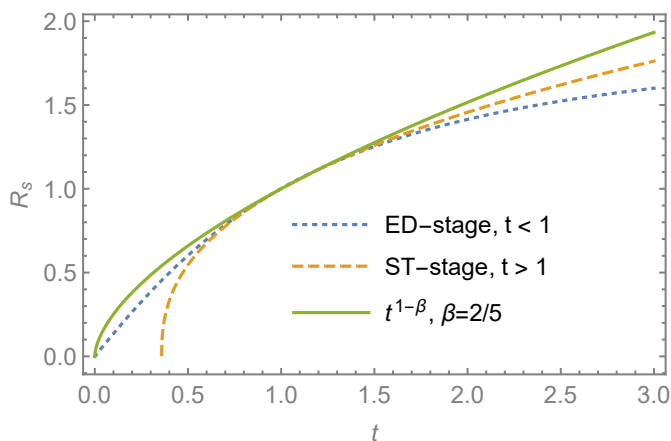


**Figure 2.** Shock radius (normalized to  $R_{ST}$ ) as a function of time (in units of  $t_{ST}$ ) shown using three different approximations, indicated on the plot.

where  $t$  is given in units of  $t_{ST}$  ( $t_0$  in our nomenclature) and  $R_{ST} \approx 0.727 M_e^{1/3} \rho_0^{-1/3} \approx 2.23 (M_e/M_\odot)^{1/3} n_0$  pc. However, most important for the CR production is perhaps the transient part between the ED and ST stages. By this epoch, the shock radius has grown large enough to process a significant amount of interstellar material while the shock is still strong enough to accelerate particles efficiently. Just a single power-law,  $R_s/R_{ST} = t^{1-\beta}$ , with  $\beta \approx 2/5$ , reproduces the transition reasonably well, by growing slower than ED but faster than ST stage. All the three approximations are shown in Fig.2. The single power-law approximation substantially deviates from the more accurate representations in eq.(4) only early in the free-expansion (ED) stage,  $t \ll t_{ST}$ , or later,  $t \gg t_{ST}$ , in the ST stage. These two regimes in the SNR expansion, however, have a less profound impact on the CR production for the reasons mentioned earlier, so we can employ

the single power-law approximation. A big advantage of this simplification is that it leads to an *exact* solution of eq.(3).

Although we will solve eq.(3) for arbitrary  $\beta$  we recapitulate that  $\beta \approx 2/5$  value is a good choice based on observations of the most popular remnants, especially the SN 1006, as shown in Table 1, also taken from McKee & Truelove (1995). The actual expansion index,  $1 - \beta$  is consistently larger than the ST value of  $1 - \beta = 0.4$  for all of the listed objects, so we will use the value  $1 - \beta = 3/5$  for the illustrations of our solution.

#### 4.3. Solution of Convection-Diffusion Equation.

##### 4.3.1. Spatial Profile

For the function  $u(z)$ , we make the conventional plane-shock assumption:  $u = -u_1$ , for  $z > 0$  and  $u = -u_2$ , for  $z \leq 0$ , where  $u_1 > u_2 > 0$ . As the shock velocity decays in time, we write

$$u = - \left( \frac{t_0}{t} \right)^\beta \begin{cases} u_1, & z > 0 \\ u_2, & z \leq 0 \end{cases}$$

In the Sedov-Taylor stage, for example,  $\beta = 3/5$ , so that the shock propagates at the speed  $U_s \propto t^{-3/5}$  and its radius grows as  $R_s \propto t^{2/5}$ .

The choice of  $\kappa_{\parallel}(p, t)$  is more difficult. Ideally, its functional form should be obtained self-consistently with the spectrum of accelerated particles, since the particle-driven turbulence determines their diffusivity. Not knowing the turbulence beforehand, we still can guess  $\kappa_{\parallel}$  on dimensional considerations. Given the shock speed  $U_s$  and its radius  $R_s$ , the only combination of the two with  $\kappa_{\parallel}$ -dimensionality is  $\kappa_{\parallel} \sim R_s U_s \propto t^{1-2\beta}$ . If we substitute  $U_s \sim 10^3 \text{ km/s}$  and  $R_s \sim 1 \text{ pc}$ , then  $\kappa_{\parallel} \sim 10^{26} \text{ cm}^2/\text{s}$ , which may be tentatively accepted as a turbulently suppressed CR diffusivity in the ISM by some two orders of magnitude. However, there are some caveats here. Not only we do not know the coefficient for  $\kappa_{\parallel}$ , but its possibly strong dependence on  $p$  is unknown. The clue comes from an obvious constraint on the highest energy particles with momentum  $p_{\text{max}}$ . They cannot diffuse in course of acceleration farther than say  $\kappa_{\parallel}(p_{\text{max}})/U_s < 0.1 R_s$ . This constraint fixes the uncertain factor at 0.1, somewhat arbitrarily but not unreasonably and, in addition, it provides some implications for  $\kappa_{\parallel}(p)$  dependence. An equivalent result can be obtained from the requirement that the acceleration time to  $p_{\text{max}}$ ,  $\tau_a \sim \kappa_{\parallel}(p_{\text{max}})/U_s^2$  is shorter than the shock dynamical time,  $R_s/U_s$  (Drury 2011). That being said, we do not need to specify the magnitude of  $\kappa_{\parallel}(p)$  as we will obtain the solution keeping it arbitrary. All we need is, by adopting the scaling  $\kappa_{\parallel} \propto U_s R_s$ , to fix the time-dependent part of the particle diffusion coefficient:

$$\kappa_{\parallel}(p, t) = \kappa(p) \left( \frac{t}{t_0} \right)^{1-2\beta}$$

Again, it is difficult to determine the  $\kappa(p)$  dependence as it is linked to the spectrum of turbulence, unknown until the particle spectrum is obtained from eq.(3). Fortunately, as we find the DSA solution for an arbitrary  $\kappa(p)$ , the two complicated problems will at least be separated.

We seek a self similar solution to eq.(3) in the following form

$$\bar{F}(t, z, p) = \phi(t, p) F(p, \xi)$$

where

$$\xi = z \left( \frac{t}{t_0} \right)^{\beta-1}.$$

For  $z, \xi \neq 0$  eq.(3) then rewrites

$$\kappa \frac{d^2 F}{d\xi^2} + (u_{1,2} + a\xi) \frac{\partial F}{\partial \xi} - \zeta F = 0 \quad (5)$$

where  $u_{1,2}$  values refer to the upstream ( $\xi \geq 0$ ) and downstream ( $\xi < 0$ ) half-space, respectively. We introduced the following two parameters

$$\zeta = \frac{t}{t_0} \frac{\partial \phi}{\phi \partial t}, \quad a = \frac{1-\beta}{t_0} \quad (6)$$

We will also use the above equation in the following form suitable for all  $\xi$

$$\kappa \frac{d^2 F}{d\xi^2} + [U(\xi) + a\xi] \frac{\partial F}{\partial \xi} - \zeta F = \frac{1}{3\phi} \frac{\partial U}{\partial \xi} p \frac{\partial}{\partial p} (\phi F) - \left( \frac{t}{t_0} \right)^{\beta} \frac{S(t)}{\phi} \delta(\xi) \delta(p - p_0) \quad (7)$$

where

$$U(\xi) = u_2 + (u_1 - u_2) H(\xi)$$

and  $H(\xi)$  is the Heaviside unit function ( $H'(x) = \delta(x)$ ). The solution of eq.(5) can be expressed in parabolic cylinder functions. To select the solutions with correct asymptotic properties upstream and downstream, it is convenient to further transform it using the following substitutions

SNR	$t/t_{\text{ST}}$	$1 - \beta$
Cas A	0.57-2.3	0.79-0.48
Kepler	0.44	0.85
Tycho	0.83	0.69
SN 1006	1.4	0.54

**Table 1.** Expansion indices and ages of selected SNRs. The data are taken from the review by McKee & Truelove (1995), where the references to the sources are provided.

$$F = g(\xi, p) \exp \left[ -\frac{\xi}{2\kappa} \left( u_{1,2} + a \frac{\xi}{2} \right) \right] = g(\eta) \exp \left[ -\frac{\eta^2}{4} + \frac{u_{1,2}^2}{4\kappa a} \right] \quad (8)$$

$$\xi = \sqrt{\kappa/a} \eta - u_{1,2}/a \quad (9)$$

which bring us to the canonical form of eq.(5)

$$\frac{\partial^2 g}{\partial \eta^2} - \left( \frac{1}{4} \eta^2 + \frac{\zeta}{a} + \frac{1}{2} \right) g = 0 \quad (10)$$

Note that the range of the new variable  $\eta$  is  $u_1/\sqrt{\kappa a} < \eta < \infty$ , upstream and  $-\infty < \eta < u_2/\sqrt{\kappa a}$  downstream. We observe that the shock coordinate  $\xi = 0$  maps to different endpoints  $\eta$  in the above intervals, because of the discontinuity in  $U(\xi)$  at  $\xi = 0$ . By denoting  $W = \eta^2/4 + \zeta/a + 1/2$ , we can write the asymptotic expressions at  $\eta \rightarrow \pm\infty$  for the two linearly independent solutions of eq.(10) as follows

$$g_{\pm} \propto \frac{1}{W^{1/4}} \exp \left( \pm \int \sqrt{W} d\eta \right)$$

Because  $F(p, \xi)$  must vanish at  $|\xi| \rightarrow \infty$ , we discard one of the solutions  $g_+$  or  $g_-$ , depending on what branch of  $\sqrt{W}$  is chosen. Thus, we must select for  $g(\eta)$  the parabolic cylinder function  $D_{\nu}(\eta)$  for  $\eta > 0$  (upstream) with the index  $\nu = -\zeta/a - 1$  (Bateman 1955). So, the solution of eq.(5) upstream ( $\eta \geq u_1/\sqrt{\kappa a}$ ) must be chosen in the form

$$F = F_u = 2D_{-\zeta/a-1}(\eta) \exp \left( -\frac{1}{4} \eta^2 \right)$$

Before writing the respective solution for the downstream medium we constrain  $\zeta/a$  parameter which allows us to simplify the solution. Indeed, according to eq.(6), we must constrain  $\phi$  by the relation  $t\partial\phi/\partial t \propto \phi$ , while  $S$  must scale with time as

$$S(t) \propto r_{cr}^2(t) Q(t) \propto R_s^2(t) U_s(t) \propto t^{2-3\beta} \quad (11)$$

Comparing this with the last term on the rhs of eq.(7), we obtain the time dependence of  $\phi$  as  $\phi \propto t^{2(1-\beta)}$ . Therefore, parameter  $\zeta/a$  is  $\zeta/a = t\dot{\phi}/(1-\beta)\phi = 2$ . For  $\zeta/a = 2$  the parabolic cylinder function and the solution upstream simplify as follows

$$\bar{F}_u = 2\phi(t, p) D_{-3}(\eta) \exp \left( -\frac{1}{4} \eta^2 \right) = \phi \left[ \sqrt{\frac{\pi}{2}} (1 + \eta^2) \operatorname{erfc} \left( \frac{\eta}{\sqrt{2}} \right) - \eta \exp \left( -\frac{1}{2} \eta^2 \right) \right] \quad (12)$$

where  $\operatorname{erfc}(x) = 1 - \operatorname{erf}(x) = (2/\sqrt{\pi}) \int_x^{\infty} \exp(-t^2) dt$  - the complementary error function. The momentum spectrum at the shock takes the form:

$$\bar{F}_0 = \phi(t, p) \left[ \sqrt{\frac{\pi}{2}} \left( 1 + \frac{u_1^2}{\kappa a} \right) \operatorname{erfc} \left( \frac{u_1}{\sqrt{2\kappa a}} \right) - \frac{u_1}{\sqrt{\kappa a}} \exp \left( -\frac{u_1^2}{2\kappa a} \right) \right] \quad (13)$$

On the downstream side of the shock we select the second linearly independent solution of eq.(10), namely  $D_{-3}(-\eta)$ , so that the solution  $\bar{F}$  downstream that matches the above expression at the shock takes the following form:

$$\bar{F}_d = 2\phi \frac{D_{-3}(u_1/\sqrt{\kappa a})}{D_{-3}(-u_2/\sqrt{\kappa a})} D_{-3}(-\eta) \exp \left( -\frac{1}{4} \eta^2 + \frac{u_2^2 - u_1^2}{4\kappa a} \right)$$

which we rewrite as

$$\bar{F}_d = \phi(t, p) \Lambda(p) \left[ \sqrt{\frac{\pi}{2}} (1 + \eta^2) \operatorname{erfc} \left( -\frac{\eta}{\sqrt{2}} \right) + \eta \exp \left( -\frac{1}{2} \eta^2 \right) \right] \quad (14)$$

with

$$\Lambda(p) \equiv \frac{\sqrt{\frac{\pi}{2}} (1 + u_1^2/\kappa a) \operatorname{erfc} (u_1/\sqrt{2\kappa a}) - (u_1/\sqrt{\kappa a}) \exp (-u_1^2/2\kappa a)}{\sqrt{\frac{\pi}{2}} (1 + u_2^2/\kappa a) \operatorname{erfc} (-u_2/\sqrt{2\kappa a}) + (u_2/\sqrt{\kappa a}) \exp (-u_2^2/2\kappa a)}$$



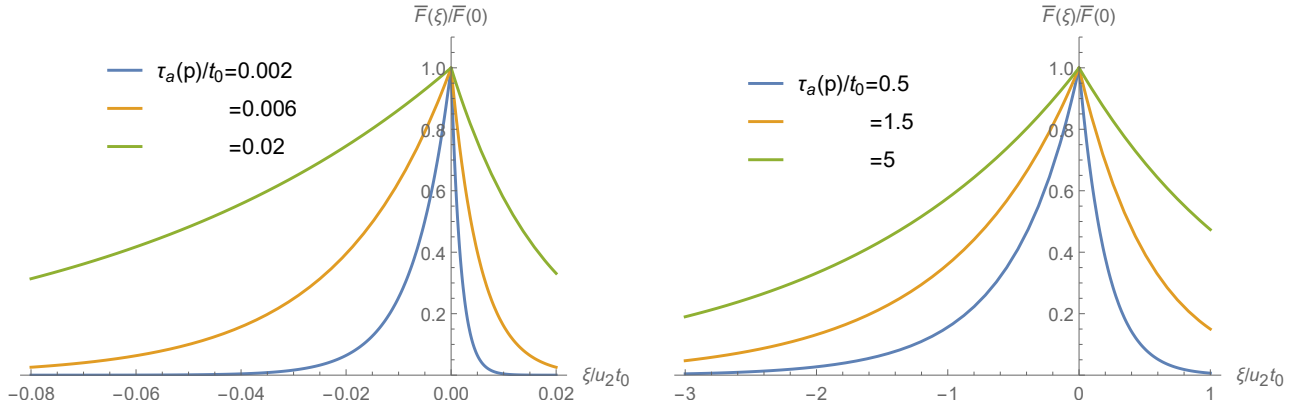


**Figure 3.** Spatial profiles of upstream and downstream particle distributions  $\bar{F}_{u,d}$  normalized to  $\bar{F}_0(p)$  (shock value), depending on the dimensionless distance from the shock front  $\xi/u_2t_0 = z/u_2t_0^{2/5}t^{3/5}$  ( $\xi > 0$ - upstream,  $\xi \leq 0$ - downstream). The left/right panel shows the profiles in the low/high -momentum range presented in the form of acceleration time to the respective momentum  $\tau_a = 2(1 - \beta)\kappa(p)/u_2^2$ .

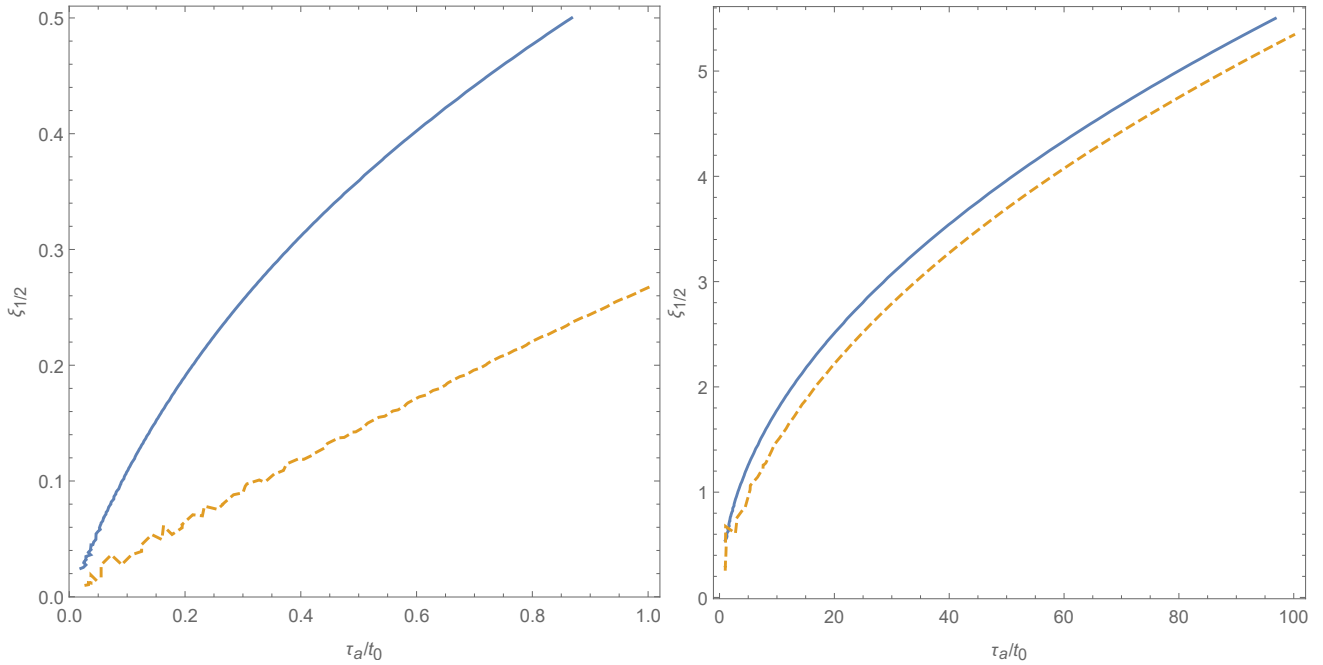


**Figure 4.** Half-width of particle distribution ( $\xi_{1/2}$ - distance from the shock where  $\bar{F}$  decreases by half from its maximum at  $\xi = 0$ ) upstream (dashed lines) and downstream (solid lines) depending on momentum, expressed in the acceleration time  $\tau_a = 2(1 - \beta)\kappa(p)/u_2^2$ .

The spatial profiles of the upstream and downstream solutions  $\bar{F}_u$  and  $\bar{F}_d$  given by eqs.(12) and (14) are shown in Fig.(3) for different particle momenta, expressed in a form of acceleration time  $\tau_a$ :

$$\tau_a = 2(1 - \beta)\kappa(p)/u_2^2 \quad (15)$$

These profiles present a notable contrast to the standard DSA solution for a steadily propagating shock which has a flat particle distribution downstream. Although a trend to a broader downstream distribution is seen in the above solution at lower momenta (more exactly, lower  $\tau_a(p)$ ), the difference between the upstream and downstream spatial extent of the particle profile diminishes at higher momenta. We emphasize this observation using Fig.4 that shows the half-width  $\xi_{1/2}$  (the distance from the front where  $\bar{F}(\xi)$  drops by 50%) for the upstream and downstream distributions, depending on momentum.

### 4.3.2. Momentum Spectrum

Turning to the momentum distribution at the shock front, we integrate eq.(7) across its velocity jump and obtain the following equation for  $\bar{F}_0(p)$ :

$$\frac{\Delta u}{3} p \frac{\partial \bar{F}_0}{\partial p} - \kappa \frac{\partial \bar{F}}{\partial \xi} \Big|_{\xi=0-}^{\xi=0+} = S(t) \left( \frac{t}{t_0} \right)^\beta \delta(p - p_0) \quad (16)$$

where  $\Delta u = u_1 - u_2$ . Introducing the following notation

$$\Phi(v) = \int_v^\infty \exp[v^2 - x^2] dx, \quad \Psi(v) = \frac{1 - 2v\Phi(v)}{(2v^2 + 1)\Phi(v) - v}, \quad v_{1,2}(p) \equiv \frac{u_{1,2}}{\sqrt{2\kappa(p)a}}$$

eq.(16) can be rewritten as follows

$$-\frac{v_1 - v_2}{3\bar{F}_0} p \frac{\partial \bar{F}_0}{\partial p} = \Psi(v_1) + \Psi(-v_2) - \frac{S(t)}{\sqrt{2a\kappa\bar{F}_0}} \left( \frac{t}{t_0} \right)^\beta \delta(p - p_0) \quad (17)$$

This relation readily provides an exact closed-form expression for the power-law index of the distribution at the shock front for  $p \geq p_0$ :

$$q(p) \equiv -\frac{p}{\bar{F}_0} \frac{\partial \bar{F}_0}{\partial p} = \frac{3\sigma}{\sigma - 1} \frac{1}{v_1} [\Psi(v_1) + \Psi(-v_2)] \quad (18)$$

where  $\sigma = u_1/u_2 = v_1/v_2$  and

$$v_2 = \frac{u_2}{\sqrt{2a\kappa(p)}} = \sqrt{\frac{t_0}{\tau_a(p)}} \quad (19)$$

The quantity  $v_2(p)$  is thus the ratio of the SN dynamic timescale  $t_0$  to the characteristic time of acceleration to the momentum  $p$ :  $\tau_a = 2(1 - \beta)\kappa(p)/u_2^2$ . The time variable formally enters the last term on the r.h.s. of eq.(17). However, we established earlier, eq.(11), that  $S \propto t^{2-3\beta}$  and  $\bar{F}_0 \propto \phi \propto t^{2(1-\beta)}$ , so  $t$  cancels out from eq.(17). By writing then  $S = S_0 (t/t_0)^{2-3\beta}$ , and using eqs.(17) and (18) we obtain the spectrum of accelerated particles at the shock front:

$$\bar{F}_0 = \frac{3S_0}{\Delta u p_0} \left( \frac{t}{t_0} \right)^{2(1-\beta)} \exp \left[ - \int_{p_0}^p q(p) \frac{dp}{p} \right] \quad (20)$$

Recall that  $\bar{F}$  is a radially integrated spectrum, according to eq.(2), so the factor  $t^{2(\beta-1)}$  is the acceleration area, since  $R_{SNR} \propto t^{1-\beta}$ . Having this at hand, the spatial distributions upstream and downstream can be obtained using eqs.(12-14). Next, we discuss the momentum spectrum and consider its two simple limits.

## 5. SPECTRAL PROPERTIES IN LIMITING CASES

The spectral index of accelerated particles in eq.(18) depends on the particle momentum through the parameter  $v_2(p) \equiv \sqrt{t_0/\tau_a(p)} \propto \kappa^{-1/2}(p)$ , which is not surprising. For the time-dependent acceleration, the dynamical timescale of the accelerator,  $t_0$ , enters the result in the form of its ratio to the acceleration time. A stationary loss-free accelerator, on the contrary, does not have any timescale, to be compared with the particle acceleration time,  $\tau_a(p)$ . Hence its spectral index is *momentum-independent*. However, in the limit  $\tau_a \ll t_0$  there should be no difference between the two cases. Indeed, we can simplify the general solution for  $q(p)$  in eq.(18) for this case and for the case of long acceleration time,  $\tau_a \gg t_0$  suitable, respectively, for low and high particle momenta. The last statement implies that the diffusion coefficient  $\kappa$  grows with  $p$ , but in general, we have imposed no restrictions on  $\kappa(p)$ . For  $v \gg 1$  (low  $p$ ) we have

$$q \approx \frac{3\sigma}{\sigma - 1} \left( 1 + \frac{3 + 2\sigma}{2\sigma^2 v_2^2} \right) \quad (21)$$

which converges to the conventional strong shock result  $q = 3\sigma/(\sigma - 1)$  when  $v_2 \rightarrow \infty$ , as expected. In the opposite case of  $v_2 \ll 1$ , one obtains

$$q = \frac{12}{\sqrt{\pi}(\sigma - 1)} \frac{1}{v_2} + 6 \left( \frac{4}{\pi} - 1 \right) \quad (22)$$

Note that the asymptotically dominant term is the first one. It is responsible for an exponential decay of the spectrum at high momenta

$$F \propto p^{-q_0} e^{-q_1(p)} \quad (23)$$

where  $q_0 = 6(4/\pi - 1)$ . Assuming the Bohm regime,  $v_2 = \sqrt{t_0/\tau_a} \propto 1/\sqrt{p}$ , for  $q_1$  we have  $q_1 = [24/\sqrt{\pi}(\sigma - 1)] \sqrt{\tau_a/t_0} \propto \sqrt{p}$ . Note that the above spectrum decays slower at high momenta than the standard DSA would for the same  $\kappa \propto p$  diffusion scaling. We will compare the two spectra in the next section. The spectral indices given by eqs.(21) and (22) are shown in Fig.5 in a strong shock limit,  $\sigma = 4$ , along with the exact result, given in eq.(18). The index  $q(\sigma, v_2)$  for arbitrary  $\sigma$  and  $v_2$  is shown in Fig.6 as a surface plot.

From these results, we conclude that even neglecting particle losses one obtains a significant spectral steepening. It is accounted for by broadening the particle injection area in time, as discussed in Sec.2, and slowing down the pace of acceleration. A more realistic treatment including the boundary losses will result in a steeper spectrum. That being said, the exponential spectral decline obtained above is significantly different from the usual DSA result. We will demonstrate this in the next section.

## 6. COMPARISON WITH STANDARD DSA

The purpose of this section is to understand whether the above modification to the DSA spectrum is a step toward reconciliation with observations. Because the “standard” DSA does not include effects addressed in this paper, it is necessary to delineate the “common territory”. According to the DSA, the spectrum terminates with a smeared cut-off, rather than a more gradual steepening described in the previous two sections. We are now poised to contrast these two spectral steepening mechanisms.

The ordinary DSA cut-off results from either a limited acceleration time or particle escape due to a finite spatial extent of acceleration region. In the first case, one can write the following equation for the maximum momentum

$$\frac{dp_{\max}}{dt} = \frac{p_{\max}}{t_{acc}} \sim \frac{p_{\max}}{\kappa(p_{\max})} U_{sh}^2(t)$$

This equation can be integrated straightforwardly, even for an arbitrary  $t_{acc}(p)$ , but it does not provide the form of the spectrum near the cut-off,  $p \sim p_{\max}$ , which we need to compare with our results. Axford (1981), for example, imposes an abrupt cut-off,  $f(p, t) \propto p^{-q_{st}} H(p_{\max}(t) - p)$  on the DSA solution with  $q_{st} = 3\sigma/(\sigma - 1)$ . Calculations that capture the spectral shape in the cutoff area (Toptygin 1980; Prishchep & Ptuskin 1981) are limited to momentum independent particle diffusivity  $\kappa$  and impose other restrictions on  $\kappa$  or the SNR expansion rate  $1 - \beta$ . In the case of momentum-independent  $\kappa$  our self-similar solution does not steepen with  $p$ , as it is subjected to the changing acceleration conditions rather than its finite duration. Including the latter effect would require a numerical solution of eq.(3) that should merely demonstrate the convergence to the self-similar solution with a time-dependent cut-off.

The second approach to the DSA termination (Blandford & Eichler 1987) is based on the particle escape, which is both better suited to our model, due to its spatial finiteness, and easier to handle. Indeed, in transforming from eq.(1) to eq.(3) we have omitted the particle escape term that we now include as follows

$$\Lambda \bar{F} + u \frac{\partial \bar{F}}{\partial z} - \frac{\partial}{\partial z} \kappa_{\parallel} \frac{\partial \bar{F}}{\partial z} = \frac{1}{3} \frac{\partial u}{\partial z} p \frac{\partial \bar{F}}{\partial p} \quad (24)$$

Here we have replaced the diffusive flux through  $r_{\perp} = r_{cr}$  by

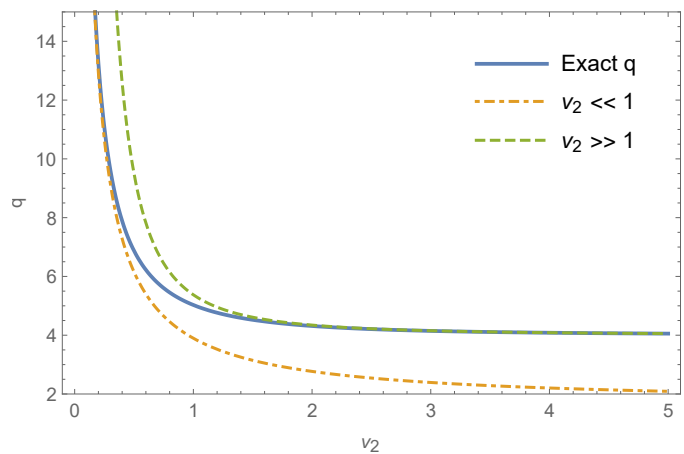


**Figure 5.** Spectral index  $q$  of accelerated particles at the shock front as a function of  $v_2 = \sqrt{t_0/\tau_a}(p)$ , as given by eqs.(18) and (19). Also shown by the dashed and dashed-dotted curves the low- and high-momentum approximations of eq.(18).

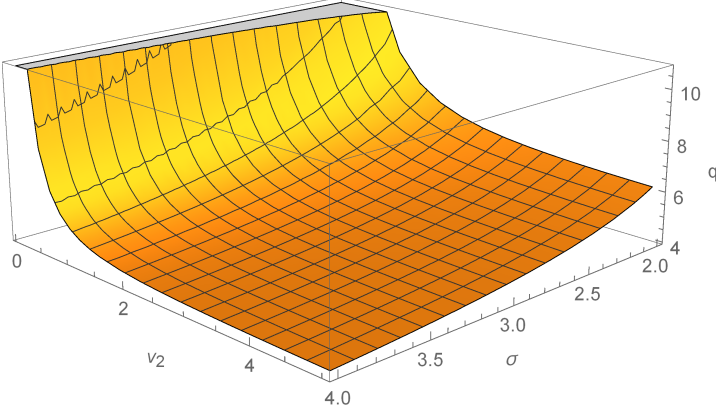


**Figure 6.** Surface plot of the spectral index  $q(\sigma, v_2)$  shown as in eq.(18).

ity jump, one obtains the following expression for the spectral slope at the shock

$$\frac{\partial \ln \bar{F}_0}{\partial \ln p} = -\frac{3}{2\Delta u} \left[ u_1 \left( 1 + \sqrt{1 + \frac{4\Lambda\kappa_{\parallel}}{u_1^2}} \right) + u_2 \left( -1 + \sqrt{1 + \frac{4\Lambda\kappa_{\parallel}}{u_2^2}} \right) \right] \quad (26)$$

Recalling that  $\Lambda \sim \kappa_{\perp}/r_{\text{cr}}^2$  we see that for the low-energy end the parameters  $\Lambda\kappa_{\parallel}/u_{1,2}^2 \sim \kappa_{\perp}\kappa_{\parallel}/r_{\text{cr}}^2 u_{1,2}^2 \ll 1$ , which is similar to the limit  $v_2 \gg 1$  in eq.(21). Note, that we can identify  $r_{\text{cr}}$  in the definition of  $\Lambda$  as  $r_{\text{cr}} \approx u_1 t_0/\sqrt{2}$ . In this limit the last results simplifies to the following

$$\frac{\partial \ln \bar{F}_0}{\partial \ln p} \approx -\frac{3u_1}{\Delta u} - 3\frac{\kappa_{\parallel}\Lambda}{\Delta u} \left( \frac{1}{u_1} + \frac{1}{u_2} \right) \quad (27)$$

The first term on the rhs represents the usual DSA slope, coinciding with the respective result in eq.(21) valid for moderate momenta where  $\kappa(p) \ll u^2 t_0$ . There is an agreement in the leading “standard DSA” term  $3\sigma/(\sigma-1)$  between eq.(21) and (27). However, the spectrum steepens significantly slower with  $p$  for the loss-dominated solution in eq.(27). Indeed, the steepening correction to the standard slope is  $\Delta q_L \sim \kappa_{\parallel}\kappa_{\perp}/r_{\text{cr}}^2 u^2 \propto \kappa_B^2 \propto p^2$ , whereas the index steepening due to the time-dependent effects, according to eq.(21) is  $\Delta q_{TD} \sim \kappa_{\parallel}/r_{\text{cr}} u \sim \sqrt{\Delta q_L} \gg \Delta q_L$ , which grows as  $p$ , assuming the Bohm diffusivity for  $\kappa_{\parallel}$ , but it may grow slower or faster than that depending on  $\kappa_{\parallel}(p)$ .

Turning to higher  $p$ , from eq.(26) we obtain

$$\frac{\partial \ln \bar{F}_0}{\partial \ln p} \approx -\frac{6}{\Delta u} \left( \sqrt{\Lambda\kappa_{\parallel}} \right) - \frac{3}{2}$$

which grows as  $p$ , whereas the respective result for the time-dependent self-similar solution shows only a  $p^{1/2}$  growth with momentum (assuming Bohm regime in both cases). It follows then that the spectrum steepening with growing momentum occurs more gradually in the case of a self-similar than steady-state solution with losses. It starts at lower momenta and continues to higher momenta without sharp termination, characteristic of the loss-dominated case.

To make a quantitative comparison, let us rewrite the expressions under the square roots in eq.(26) as  $4\Lambda\kappa_{\parallel} = \rho p^2$ , as to a good approximation  $\kappa_{\parallel}\kappa_{\perp} \approx \kappa_B^2 \propto p^2$  (so  $\rho = 4\kappa'_{\parallel}\kappa'_{\perp}/r_{\text{cr}}^2$ , where prime denotes  $\partial_p$ ). Now we integrate this equation and obtain the following spectrum at the shock

$$\bar{F}_0 = \frac{C'}{p^{3\sigma/(\sigma-1)}} \left[ u_1 + \sqrt{u_1^2 + \rho p^2} \right]^{\frac{3\sigma}{2(\sigma-1)}} \left[ u_2 + \sqrt{u_2^2 + \rho p^2} \right]^{\frac{3}{2(\sigma-1)}} \exp \left[ -\frac{3}{2\Delta u} \left( \sqrt{u_1^2 + \rho p^2} + \sqrt{u_2^2 + \rho p^2} \right) \right] \quad (28)$$

To compare the last result with the self-similar time-dependent solution given by eqs.(18) and (20), it is convenient to use the following dimensionless momentum

$$\mathcal{P} = \sqrt{\rho} p / u_2 = 2^{3/2} \kappa_B / R_s u_2$$

$$-r\kappa_{\perp} \left. \frac{\partial f}{\partial r} \right|_{r=r_{\text{cr}}} = \Lambda \bar{F} \quad (25)$$

and we will use  $\Lambda \sim \kappa_{\perp}/r_{\text{cr}}^2$  for an estimate. The above formula is a direct analog of the Newton’s law for a flux (e.g., thermal) at an interface between two media (here at  $r = r_{\text{cr}}$ ). We have neglected the time derivative, as the spectrum is expected to be nearly stationary near the cut-off momentum, since the acceleration should be balanced by particle losses. For the same reason, the flow velocity and particle diffusivity can also be considered fixed in time at their current values. The particle injection term is irrelevant at these energies and therefore omitted. Solving the above equation upstream and downstream with  $u = -u_{1,2}$ , and integrating it across the velocity

Note that the variable  $v_2$ , used in eq.(19) can be expressed through  $\mathcal{P}$  as

$$v_2 = \frac{2^{1/4}}{\sqrt{\sigma(1-\beta)\mathcal{P}}}, \quad (29)$$

assuming the Bohm diffusion scaling for  $\kappa(p)$  in eq.(18). Again, it is not the purpose of this comparison to obtain an exact position of the cut-off in the standard DSA spectrum, but rather its momentum profile; so we consider  $u_1$  and  $R_s$  “frozen” and put  $R_s \approx u_1 t_0$ . Meanwhile, eq.(28) rewrites

$$\bar{F}_0 = \frac{C}{\mathcal{P}^{3\sigma/(\sigma-1)}} \left[ \sigma + \sqrt{\sigma^2 + \mathcal{P}^2} \right]^{\frac{3\sigma}{2(\sigma-1)}} \left[ 1 + \sqrt{1 + \mathcal{P}^2} \right]^{\frac{3}{2(\sigma-1)}} \exp \left[ -\frac{3}{2(\sigma-1)} \left( \sqrt{\sigma^2 + \mathcal{P}^2} + \sqrt{1 + \mathcal{P}^2} \right) \right] \quad (30)$$

After adjusting the normalization factors in eqs.(20) and (30), both results are shown in Fig.7, extending the limiting case estimates above to a broader momentum range. We have placed the DSA solutions with quite different mechanisms of spectral steepening (particle escape vs shock expansion) on one plot to emphasize the difference in their spectral shapes.

The particle loss model employed above, shapes the form of the standard DSA spectral cut-off through the product  $\kappa_{\parallel}\kappa_{\perp}$ , which is firmly bound to  $\kappa_B^2(p)$ , according to the widely accepted anisotropic diffusion paradigm, e.g., (Drury 1983). This relation significantly constrains the standard DSA in explaining the observed steep spectra. By contrast, the solution obtained in this paper depends on  $\kappa_{\parallel}(p)$ , and in the particular case of Bohm diffusion, it is characterized by a more gradual steepening at high energies, Fig.7. Only for  $\kappa_{\parallel} \propto p^2$ , the functional form of the rollover is similar to the DSA cut-off (see below). Generally,  $\kappa_{\parallel}(p)$  strongly depends on the turbulence model in use. We explore the potential of the present solution to explain observed spectra by replacing the Bohm diffusion in Fig.7 with the three different turbulence models, often used in conjunction with CR acceleration and propagation (Blasi & Amato 2012; Ptuskin 2012). These are the Kolmogorov model, with  $\kappa \propto p^{1/3}$ , Kraichnan model with  $\kappa \propto p^{1/2}$  and the short-scale non-resonant turbulence model due to Bell instability with the diffusivity scaling  $\kappa \propto p^2$ . These three and the Bohm model are compared in Fig.8 with a DSA result, first without cutoff. Assuming then that the relation  $\kappa_{\parallel}\kappa_{\perp} \approx \kappa_B^2$  holds up also at the edge of the acceleration zone, where the CR diffusion is expected to be strongly anisotropic with  $\kappa_{\parallel} \gg \kappa_{\perp}$ , we impose the DSA cut-off profile, eq.(30), on the turbulent transport models listed above. The results are shown in Fig.9 with a warning that, by contrast to the spectra shown in Fig.8, the solutions with the imposed cut-offs are no longer the exact loss-free solutions of eq.(3)

Although the mechanism of spectral steepening suggested in this paper and the spectrum termination in the standard DSA invoke different physical phenomena, the above comparison of the results may be helpful in analyzing the emission spectra from bilateral SNRs and understanding the production of bulk CR spectra. Specifically, if an observed spectrum exhibits a gradual decline rather than a sharp one, it is more likely that the steepening mechanisms considered in this paper are at work and the cut-off is simply not reached yet. An improved approach would be an incorporation of the lateral CR escape flux in our treatment of Sec.4.3. However, the main difficulty that remains is an accurate calculation of the loss function  $\Lambda$ . It requires a solution of a two-dimensional CR transport problem at an interface between domains of strongly different propagation regimes. Even if inside of the acceleration zone,  $r_{\perp} < r_{\text{cr}}$ ,  $|z| \lesssim \kappa/u$  one may put  $\kappa_{\parallel} \approx \kappa_{\perp} \approx \kappa_B(p)$ , for  $r > r_{\text{cr}}$  the CR transport regime becomes strongly anisotropic with  $\kappa_{\parallel} \gg \kappa_{\perp}$ .

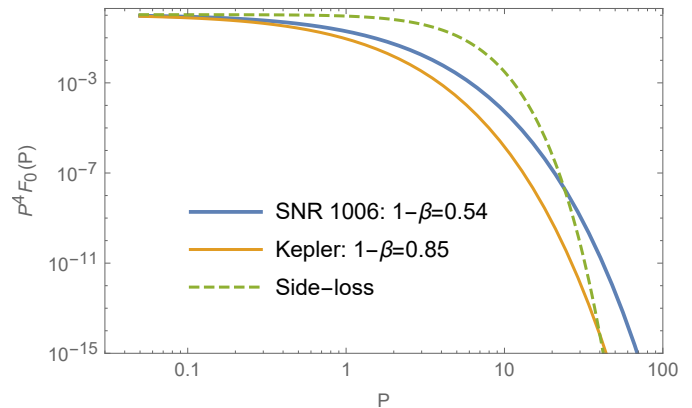


**Figure 7.** Solid lines: loss-free spectrum from self-similar solution for indicated values of expansion index  $1 - \beta$  and Bohm diffusion. Dashed line: stationary solution with sideways losses. Both solutions are given using normalized momentum  $\mathcal{P} = 2^{3/2}\kappa_B/R_s u_2$ . The standard DSA solution with particle losses implies that  $\kappa_{\parallel}\kappa_{\perp} \propto \kappa_B^2 \propto p^2$  (see text). The shock compression  $\sigma = 4$  and the spectra are multiplied by  $p^4$ .

## 7. SUMMARY

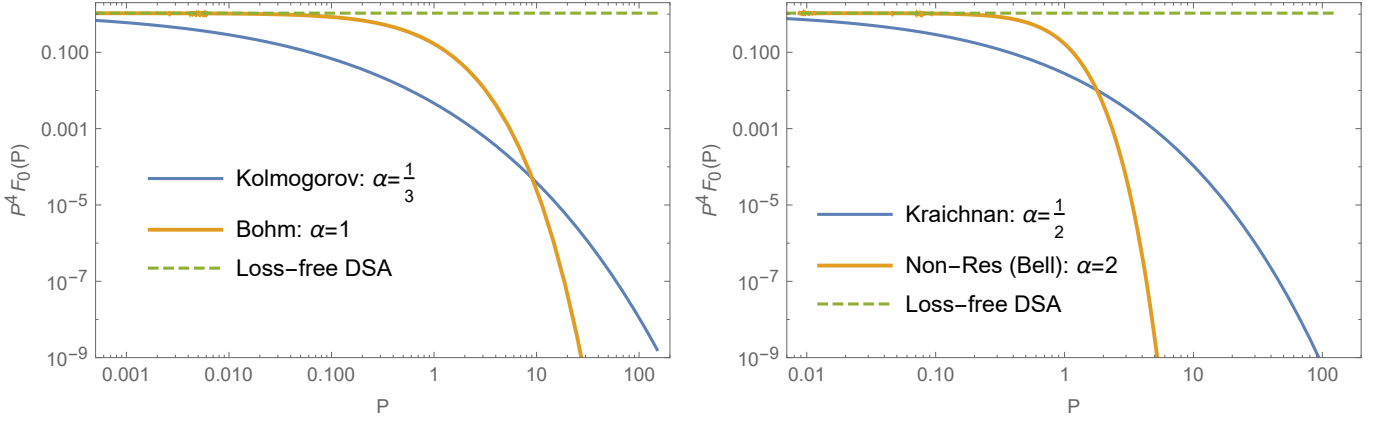


**Figure 8.** The same as in Fig.7, but for different turbulence models (solid lines) and for the expansion index  $1 - \beta = 3/5$  (see Fig.2). The standard DSA solution is shown for comparison on both panels (dashed lines) without cut-off.

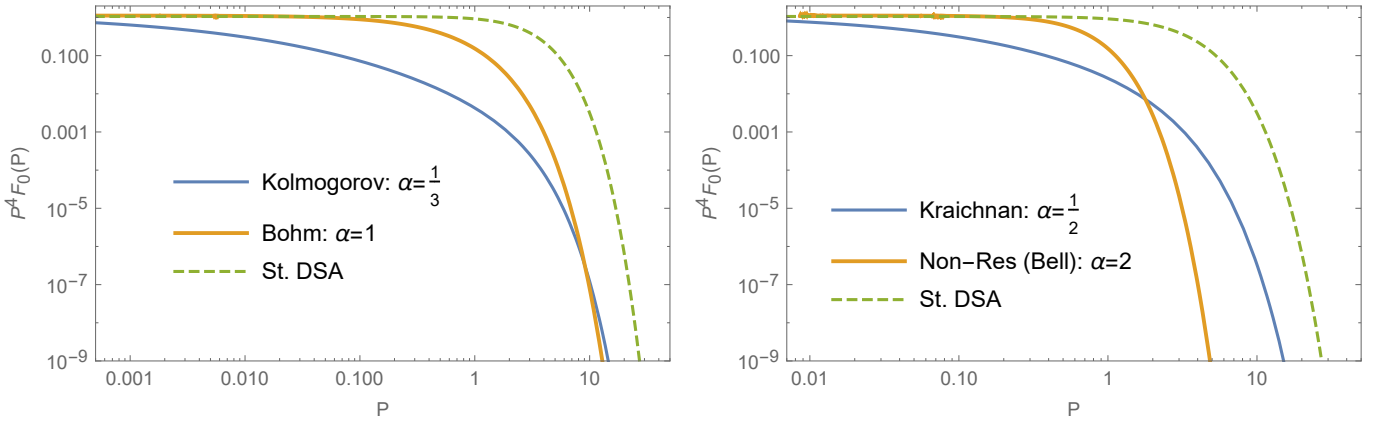


**Figure 9.** The same spectra as in Fig.8 but with cut-offs imposed on all three spectra using the functional form obtained for the standard DSA in eq.(30).

In this paper, we have investigated the DSA operation in a spherical SNR shock expanding in a homogeneous magnetic field. We have obtained an exact self-similar solution for an arbitrary shock expansion index,  $1 - \beta$ , (defined as  $R_{SNR} \propto t^{1-\beta}$ ), and particle diffusivity  $\kappa(p)$ . Particle injection was assumed to be efficient on two polar caps where the shock normal is inline with the magnetic field within  $\simeq 45^\circ$ . Possible losses of particles from the acceleration regions were neglected, except for a comparison with the conventional DSA solution. The salient features of the new solution are:

- particle momentum spectrum at the shock depends on the ratio of acceleration time,  $\tau_a \sim \kappa(p)/U_{sh}^2$  to the SNR dynamic time  $t_0$  which, in turn, is related to the shock expansion as  $R_{SNR}(t) = R_{ST}(t/t_0)^{1-\beta}$ , or  $U_{sh}(t) = u_1(t_0/t)^\beta$  (sec.4.2)
  - for  $\tau_a \ll t_0$ , the spectrum has the standard DSA index determined by the shock compression,  $\sigma$ , that is  $f \propto p^{-q}$ , with  $q = 3\sigma/(\sigma - 1)$
  - the spectral index increases at larger  $\tau_a$ , and for  $\tau_a \gg t_0$  it is suppressed by an exponential factor  $\exp[-C\sqrt{\tau_a(p)/t_0}]$ , where  $C(\sigma) \approx 4.5$ , eq.(23)
  - this factor decreases with momentum much slower than the conventional DSA cutoff, obtained, e.g., for the cross-field losses from the acceleration zone of size  $r_{cr} \propto \exp[-6\kappa_B(p)/\Delta u r_{cr}]$ , eq.(30)
- the spatial distributions of particles upstream and downstream are significantly different only at lower energies, with the downstream distribution being broader, as in the planar shock solutions, Fig.3

- at higher energies ( $\tau_a(p) \gg t_0$ ) the upstream and downstream acceleration zones are nearly equal, Fig.4, thus making a strong contrast to the plane-shock and spherically symmetric (e.g., Kang et al. (2013)) solutions

## 8. DISCUSSION

There may be several reasons why the CR spectrum predicted by the DSA disagrees with SNR observations and with the spectra of CRs arriving at the Earth’s atmosphere. We have shown that relaxing the shock stationarity and spherical symmetry assumptions, typical of DSA models, alters the following two DSA predictions. First, the SNR evolution affects the acceleration stronger than in a spherically symmetric case because the active acceleration zone on the shock grows in time while not covering the entire shock surface. The growth time is the SNR dynamic time  $t_0$  and it affects the spectrum even well below the cut-off. The latter is generally determined by the total duration of acceleration,  $t_{SNR}$ , shock size, and the level of magnetic field amplification. Of course, these three factors will set the ultimate cut-off energy also for the present solution. Below that, the spectrum rolls over when the particle acceleration time to momentum  $p$ ,  $\tau_a(p) \sim \kappa(p)/U_{sh}^2$ , becomes comparable with  $t_0$ . In historical SNRs from Table 1,  $t_0 > t_{SNR}$  except for the SNR 1006. Generally, the condition  $t_0 < t_{SNR}$  must hold for the self-similar solution to establish at high energies where  $\tau_a(p) > t_0$ . This condition can be relaxed if the maximum momentum is limited on physical grounds (e.g., losses) to  $\tau(p_{max}) < t_{SNR}$ . In this paper we have imposed a cut-off,  $p_{max}$ , only for comparison with the standard DSA solution.

The second modification to the DSA is that accelerated particles stay closer to the shock than in the “standard” planar and spherically symmetric solutions. This effect is related to the growing surface of acceleration that restricts particle convection time downstream. It is more pronounced for high-energy particles since they spent most of the time near the shock to gain high energy. The difference can be seen by comparing Figs.3 and 4 with the numerical solutions for a spherically symmetric acceleration performed earlier, e.g., by Kang et al. (2013). This result may have implications for the interpretation of thin x-ray filaments observed in the SNR 1006 in particular (Bamba et al. 2005; Long et al. 2003).

Although the solution obtained in this paper strictly applies to the bilateral shock morphology, effects of changing magnetic field inclination may be significant for the DSA in SNRs expanding in more complicated magnetic environments. The SNR RX J 1713, for example, does not belong to the bilateral type but it shows a patchy pattern of particle acceleration around its rim (H. E. S. S. Collaboration et al. 2018). This may be an effect of ambient gas density, but it may be produced by variable field inclination as well. Young SNRs usually have a radial field at the shock front (Dickel et al. 1991; West et al. 2017; Vink & Zhou 2018), but the radial field geometry is most probably a result of particle acceleration rather than its prerequisite. Such SNRs may have started accelerating particles from either bilateral state or from multiple hot spots (where  $\vartheta_{nB} \lesssim \pi/4$ ) that merge later. While this scenario is just a speculation, it is not obvious how else one can reconcile the radial field morphology all around the rim with an arbitrary, possibly homogeneous initial field into which the progenitor star has exploded. The SNR 1006 is, perhaps, a telltale counterexample to the puzzling omni-radial field geometry of young remnants.

### 8.1. Acceleration Nonlinearity and Turbulent Heating

The nonlinear shock modification, mentioned in the Introduction, is often considered as irrelevant to the SNR shocks for the following two reasons. First, it predicts flatter than the linear DSA spectra, not steeper ones, as suggested by observations (see Malkov & Drury 2001 for a review of nonlinear solutions). Second, it is not observed in hybrid simulations. We believe that neither argument is convincing. Starting from the apparent problem with the observations, our new solution that steepens at high energies can easily compensate for the nonlinear flattening. It is also impossible to ignore the fact that the nonlinear DSA regime follows *directly* from equations describing the acceleration. The exact criteria for transitioning of the acceleration to the nonlinear regime can be obtained from a bifurcation analysis of the steady-state kinetic solution. This solution links the problem parameters, discussed below, by placing them on a surface in the multidimensional parameter space. The solution, however, needs to be obtained in analytic form to understand the transition since it is unstable on a certain part of that surface and thus inaccessible for numerical or “semi-analytic” approaches.

The *critical* parameters characterizing the transition are (i) injection rate of thermal particles (roughly a fraction of accelerated CRs,  $\eta$ ), (ii) shock Mach number,  $M$ , (iii) maximum momentum,  $p_{max}$ , and (iv) heating rate of the upstream plasma. While the parameters (i-iii) are usually reasonably known (with some reservations about  $p_{max}$ ,

discussed below), the heating rate is a highly uncertain parameter. A zero-order approximation of the (i-iii) part of the parameter space where the acceleration must be in an efficient nonlinear regime is the following:  $p_{\max}/m_p c \gtrsim 10^3$ ,  $M \gtrsim 20$ , and the injection rate  $\eta \gtrsim 10^{-3}$ . Each of these thresholds can be lowered somewhat at the expense of the other two. However, the maximum momentum cannot be significantly decreased, since the requirement for the nonlinear transition, which is in fact  $\ln(p_{\max}/mc) \gg 1$ , simply follows from the scaling of the CR pressure,  $P_{CR}$ , with  $p_{\max}$ . In a pre-transition test-particle acceleration regime, when the CR spectrum is  $\propto p^{-4}$ , the CR pressure grows slowly with  $p_{\max}$ , namely,  $P_{CR} \propto \eta \ln(p_{\max}/m_p c)$ . Since  $P_{CR}$  must become comparable to the shock ram pressure for the transition to occur, and since  $\eta \ll 1$ , the required  $p_{\max}$  is quite high and not yet attainable in the current hybrid, let alone PIC simulations. Not surprisingly, the nonlinear transition is not observed in such simulations. Of course, it is inexorably present to all numerical solutions satisfying the above set of criteria, e.g., (Kang & Jones 2002).

Meanwhile, upon transitioning to the nonlinear acceleration regime, the spectrum becomes much flatter,  $\propto p^{-3.5}$ , so that the CR pressure grows much sharper with  $p_{\max}$ ,  $P_{CR} \propto p_{\max}^{1/2}$ . It is this feedback loop connecting the CR pressure and the spectral index that makes a hard (hysteresis type) transition to the nonlinear acceleration regime. Under these circumstances, the heating must be provided by a collisionless turbulence dissipation (via plasma microinstabilities) in the upstream flow permeated by the CRs. They drive strong turbulence, and a complicated coupling to the driver (CRs) exacerbates the problem of turbulence dissipation. There are no analytic studies that quantitatively address this problem. Since scales associated with large gyroradii of particles at highest energies are immensely disparate, the problem is not tractable numerically either. Therefore, the heating rate of the upstream plasma remains largely unknown.

Not having a reliable heating rate at hand, we can still parameterize it and obtain the nonlinear solution for the DSA. This solution, shown in Fig.6 of (Malkov & Drury 2001), proves very sensitive to that same heating rate. For example, if we decrease this parameter by about two orders of magnitude across its high-sensitivity range, the spectrum will change from a pure test particle,  $f \propto p^{-4}$ , to strongly nonlinear,  $f \propto p^{-3.5}$ . Note that these are the limiting cases with vastly different acceleration efficiencies. In the latter case, most of the particle pressure is deposited near  $p_{\max}$ , which appears to be inconsistent with the continuous spectrum steepening obtained in this paper. Indeed, it must diminish the nonlinear effects by restricting the growth of an *effective*  $p_{\max}$  that controls the nonlinear transition. However, appealing to our discussion of the spectrum steepening illustrated by Fig.1 we can reconcile the opposite trends. First of all, the nonlinear transition must begin in the area (near magnetic axis) with the longest acceleration history where the local value of  $p_{\max}$  is higher. In the outskirts of the acceleration zone, recently injected particles with much lower  $p_{\max}$  will dominate the spectrum. As we already argued earlier, the line-of-sight- or acceleration-zone-averaged spectrum must appear as a superposition of these two extremes. Therefore, the nonlinear hardening of the central spectrum will be masked by the softer periphery.

Apart from the above-discussed variation of the spectrum along the shock surface, an intrinsic time dependence of nonlinear acceleration should also play an important role in establishing the integrated spectrum. This variability occurs independently of the spherical shock effects, addressed in this paper. As we argued above, the nonlinear transition to an efficient acceleration regime is quasi-abrupt in character. It occurs when  $p_{\max}(t)$  surpasses its critical value. Soon thereafter, an increased CR pressure reacts back on the shock structure thereby decreasing the injection and increasing heating rate, thus driving the system back to its subcritical state. The backtransition is, however, not sustainable since  $p_{\max}$  continues to grow, so the next forward transition must follow. These limit-cycle oscillations have been *predicted* from the analytic solution of the nonlinear acceleration problem. Indeed, they appear to be present in numerical solutions due to Kang & Jones (2002) (see their Fig.7 and a recent discussion of the phenomenon by Malkov 2018). As in the case of spatial variation of acceleration efficiency, the limit-cycle oscillations must result in a spectral index between its efficient and test-particle values. Since the steepening of the test-particle solution obtained in the present paper is significant, the net result may be in the ballpark of the current observations (Aharonian et al. 2018). Again, the quantitative predictions require a resolution of complicated issues associated with particle losses and turbulent heating efficiency.

## 8.2. Concluding Remarks

With all the above limitations in mind, we may still ask how important for the integrated CR spectrum the obtained solution might be. To answer this question, in addition to more realistic particle losses discussed in the Introduction, one needs to self-consistently include the particle injection rate,  $Q$ , and, most importantly, their diffusion coefficient  $\kappa(p)$  into the obtained spectrum. A promising strategy is to extract these acceleration parameters from the hybrid



(and therefore *very* limited-time) shock simulation, taken at a *few* short SNR evolution periods, and interpolate them in the solution obtained above. Using a similar approach [Hanusch et al. \(2019\)](#) recently provided a viable explanation of the anomaly of proton/Helium ratio rigidity spectrum, presumably accumulated over the free-expansion to Sedov-Taylor SNR stages. It is important to understand, that the p/He *ratio* rigidity spectrum is not changed by the spectral hardening or softening described above, or by any other electromagnetic processes, such as propagation in, or escape from, the galaxy.

Returning to the spectrum softening mechanism suggested in this paper and looking at Fig.8 one may come to a disappointing conclusion. By adjusting the CR diffusion model for  $\kappa(p)$  within a range between Kolmogorov and non-resonant small-scale (Bell) turbulence one can fit almost any observed spectrum. On the bright side, we obtained liberation from the notoriously inflexible linear DSA spectrum that is increasingly in conflict with the rapidly improving observations. Moreover, while the soft  $\gamma$ -ray spectra of young SNR can be explained within the standard (linear or non-linear) DSA framework only by introducing "early" cutoffs<sup>2</sup>, Fig.8 shows that the approach described in this paper may explain them without a commonly assumed and in practice inevitably parameterized exponential cutoff! The  $\kappa$ -dependence on energy naturally produces a more gradual decay of the spectrum. This implies, in particular, that the steep spectra of SN 1006, Tycho, Cas A, RX J 1713 (see [Aharonian et al. 2018](#) for further discussion and references), as reported in the multi-TeV energy band, cannot rule out these objects as PeVatrons. Whether the highest-energy particles in these SNRs can reach the PeV range in detectable numbers, is a different issue falling outside the scope of this paper.

Work of MM is supported by NASA Astrophysics Theory Program under grant 80NSSC17K0255.

<sup>2</sup> There are alternative spectral softening mechanisms, e.g. ([Malkov & Diamond 2006](#)), not discussed here because they require non-diffusive particle transport, thus departing from the convection-diffusion equation ([Kirk et al. 1996](#); [Zimbardo & Perri 2013](#)) (see, however, conclusions in ([Malkov 2017](#)) regarding some issues with the justification of non-diffusive CR transport).

## REFERENCES

- Aharonian, F., Yang, R., & de Oña Wilhelmi, E. 2018, ArXiv e-prints. <https://arxiv.org/abs/1804.02331>
- Axford, W. I. 1981, International Cosmic Ray Conference, 12, 155
- Bamba, A., Yamazaki, R., Yoshida, T., Terasawa, T., & Koyama, K. 2005, *Astrophys. J.* , 621, 793, doi: [10.1086/427620](https://doi.org/10.1086/427620)
- Bateman, H. 1955, Higher transcendental functions
- Bell, A. R., Matthews, J. H., & Blundell, K. M. 2019, arxiv: 1906.12240, to appear in MNRAS
- Berezhko, E. G., Yelshin, V. K., & Ksenofontov, L. T. 1994, *Astroparticle Physics*, 2, 215, doi: [10.1016/0927-6505\(94\)90043-4](https://doi.org/10.1016/0927-6505(94)90043-4)
- Bisnovatyi-Kogan, G. S., & Silich, S. A. 1995, *Reviews of Modern Physics*, 67, 661, doi: [10.1103/RevModPhys.67.661](https://doi.org/10.1103/RevModPhys.67.661)
- Blandford, R., & Eichler, D. 1987, *Phys. Rep.* , 154, 1
- Blasi, P., & Amato, E. 2012, *Journal of Cosmology and Astroparticle Physics*, 2012, 010
- Caprioli, D., & Spitkovsky, A. 2014, *Astrophys. J.* , 783, 91, doi: [10.1088/0004-637X/783/2/91](https://doi.org/10.1088/0004-637X/783/2/91)
- Cassam-Chenaï, G., Hughes, J. P., Reynoso, E. M., Badenes, C., & Moffett, D. 2008, *Astrophys. J.* , 680, 1180, doi: [10.1086/588015](https://doi.org/10.1086/588015)
- Chevalier, R. A. 1977, *Ann. Rev. Astron. Astroph.* , 15, 175, doi: [10.1146/annurev.aa.15.090177.001135](https://doi.org/10.1146/annurev.aa.15.090177.001135)
- D'Angelo, M., Blasi, P., & Amato, E. 2016, *Phys. Rev. D* , 94, 083003, doi: [10.1103/PhysRevD.94.083003](https://doi.org/10.1103/PhysRevD.94.083003)
- Dickel, J. R., van Breugel, W. J. M., & Strom, R. G. 1991, *AJ*, 101, 2151, doi: [10.1086/115837](https://doi.org/10.1086/115837)
- Drury, L. O. 1983, *Reports on Progress in Physics*, 46, 973
- . 2011, *Mon. Not. R. Astron. Soc.* , 415, 1807, doi: [10.1111/j.1365-2966.2011.18824.x](https://doi.org/10.1111/j.1365-2966.2011.18824.x)
- Ellison, D. C., Baring, M. G., & Jones, F. C. 1995, *Astrophys. J.* , 453, 873, doi: [10.1086/176447](https://doi.org/10.1086/176447)
- Gabici, S., Evoli, C., Gaggero, D., et al. 2019, arXiv e-prints, arXiv:1903.11584. <https://arxiv.org/abs/1903.11584>
- H. E. S. S. Collaboration, Abdalla, H., Abramowski, A., et al. 2018, *Astronomy and Astrophys.*, 612, A6, doi: [10.1051/0004-6361/201629790](https://doi.org/10.1051/0004-6361/201629790)
- Hanusch, A., Liseykina, T. V., & Malkov, M. 2019, *Astrophys. J.* , 872, 108, doi: [10.3847/1538-4357/aafdae](https://doi.org/10.3847/1538-4357/aafdae)
- Kang, H., & Jones, T. W. 2002, *Journal of Korean Astronomical Society*, 35, 159, doi: [10.5303/JKAS.2002.35.4.159](https://doi.org/10.5303/JKAS.2002.35.4.159)
- Kang, H., Jones, T. W., & Edmon, P. P. 2013, *Astrophys. J.* , 777, 25, doi: [10.1088/0004-637X/777/1/25](https://doi.org/10.1088/0004-637X/777/1/25)
- Kirk, J. G., Duffy, P., & Gallant, Y. A. 1996, *Astronomy and Astrophys.*, 314, 1010
- Long, K. S., Reynolds, S. P., Raymond, J. C., et al. 2003, *Astrophys. J.* , 586, 1162, doi: [10.1086/367832](https://doi.org/10.1086/367832)
- Malkov, M. 2018, *Nuclear and Particle Physics Proceedings*, 297-299, 20 , doi: <https://doi.org/10.1016/j.nuclphysbps.2018.07.004>
- Malkov, M. A. 2017, *Physical Review D*, 95, 023007
- Malkov, M. A., & Diamond, P. H. 2006, *Astrophys. J.* , 642, 244, doi: [10.1086/430344](https://doi.org/10.1086/430344)
- Malkov, M. A., Diamond, P. H., Sagdeev, R. Z., Aharonian, F. A., & Moskalenko, I. V. 2013, *Astrophys. J.* , 768, 73, doi: [10.1088/0004-637X/768/1/73](https://doi.org/10.1088/0004-637X/768/1/73)
- Malkov, M. A., & Drury, L. O. 2001, *Reports on Progress in Physics*, 64, 429
- Malkov, M. A., & Völk, H. J. 1995, *Astronomy and Astrophys.*, 300, 605
- McKee, C. F., & Truelove, J. K. 1995, *Phys. Rep.* , 256, 157, doi: [10.1016/0370-1573\(94\)00106-D](https://doi.org/10.1016/0370-1573(94)00106-D)
- Nava, L., & Gabici, S. 2013, *Mon. Not. R. Astron. Soc.* , 355, doi: [10.1093/mnras/sts450](https://doi.org/10.1093/mnras/sts450)
- Pais, M., Pfrommer, C., Ehlert, K., & Pakmor, R. 2018, *Mon. Not. R. Astron. Soc.* , 478, 5278, doi: [10.1093/mnras/sty1410](https://doi.org/10.1093/mnras/sty1410)
- Prishchep, V. L., & Ptuskin, V. S. 1981, *AZh*, 58, 779
- Ptuskin, V. 2012, *Astroparticle Physics*, 39, 44, doi: [10.1016/j.astropartphys.2011.11.004](https://doi.org/10.1016/j.astropartphys.2011.11.004)
- Thomas, V., & Winske, D. 1990, *Geophysical Research Letters*, 17, 1247
- Toptygin, I. N. 1980, *Space Science Reviews*, 26, 157
- Vink, J., & Zhou, P. 2018, *Galaxies*, 6, 46, doi: [10.3390/galaxies6020046](https://doi.org/10.3390/galaxies6020046)
- Völk, H. J., Berezhko, E. G., & Ksenofontov, L. T. 2003, *Astronomy and Astrophys.*, 409, 563, doi: [10.1051/0004-6361:20031082](https://doi.org/10.1051/0004-6361:20031082)
- West, J. L., Jaffe, T., Ferrand, G., Safi-Harb, S., & Gaensler, B. M. 2017, *Astrophys. J. Lett.* , 849, L22, doi: [10.3847/2041-8213/aa94c4](https://doi.org/10.3847/2041-8213/aa94c4)
- Zimbaro, G., & Perri, S. 2013, *Astrophys. J.* , 778, 35, doi: [10.1088/0004-637X/778/1/35](https://doi.org/10.1088/0004-637X/778/1/35)